QUANTUM GENERATOR KERNELS

Anonymous authors
Paper under double-blind review

ABSTRACT

Quantum kernel methods offer significant theoretical benefits by rendering classically inseparable features separable in quantum space. Yet, the practical application of *Quantum Machine Learning* (QML), currently constrained by the limitations of *Noisy Intermediate-Scale Quantum* (NISQ) hardware, necessitates effective strategies to compress and embed large-scale real-world data like images into the constrained capacities of existing quantum devices or simulators. To this end, we propose *Quantum Generator Kernels* (QGKs), a generator-based approach to quantum kernels, comprising a set of *Variational Generator Groups* (VGGs) that merge universal generators into a parameterizable operator, ensuring scalable coverage of the available quantum space. Thereby, we address shortcomings of current leading strategies employing hybrid architectures, which might prevent exploiting quantum computing's full potential due to fixed intermediate embedding processes. To optimize the kernel alignment to the target domain, we train a weight vector to parameterize the projection of the VGGs in the current data context. Our empirical results demonstrate superior projection and classification capabilities of the QGK compared to state-of-the-art quantum and classical kernel approaches and show its potential to serve as a versatile framework for various QML applications.

1 INTRODUCTION

Quantum computing offers fundamentally new paradigms for machine learning by exploiting quantum properties such as superposition and entanglement (Preskill, 2018; Biamonte et al., 2017). Among these, quantum kernel methods have shown promise for enhancing data separability via expressive feature maps that operate in high-dimensional Hilbert spaces, allowing them to capture structures that classical kernels cannot efficiently represent (Schuld & Killoran, 2019). Despite these theoretical promises, the practical application of QML is currently limited by the capabilities of NISQ devices, which are still in their developmental stages (Preskill, 2018). Still limited in qubit capacities and subject to errors, embedding large-scale data into quantum devices is a significant hurdle that must be overcome to exploit the full potential of QML. Hybrid QML architectures bridge this gap, using classical pre-processing to embed data into quantum systems (Cerezo et al., 2021). However, recent studies also highlight key limitations: many current approaches rely on fixed embeddings that do not scale well with high-dimensional inputs and are susceptible to barren plateaus during training (McClean et al., 2018). Addressing this requires scalable, flexible, and learnable quantum embeddings that can exploit these properties while remaining parameter-efficient and robust to noisy hardware.

In this work, we propose a novel kernel architecture grounded in Lie algebraic generators, aggregated into parameterizable groups that project input data directly into quantum space. Our approach can be broken down into three steps: Construct a set of generators and merge them into *Variational Generator Groups* (VGGs). We refer to a set of these groups as the *Quantum Generator Kernel* (QGK), which is executed by its set of operators. To improve alignment between data and the resulting kernel, we introduce a linear feature extractor that is pre-trained to project high-dimensional input into a compressed generator space. Unlike previous methods that rely on static gate-based embeddings, our QGK architecture employs Hamiltonian-driven unitaries with learnable generator weights, enabling expressive and scalable data encoding. By projecting high-dimensional data into a compact generator-weighted space, QGKs achieve high parameter efficiency per qubit and flexible embedding capacity, while effectively leveraging the expressive power of the full Hilbert space. We validate the QGK both analytically and empirically: theoretical analyses confirm its expressivity and

scalability, while experimental results demonstrate superior classification accuracy and robustness to noise across synthetic and real-world benchmarks. We summarize our contributions as follows:

- We introduce *Variational Generator Groups* (VGGs), which aggregate a universal set of Lie algebraic generators into parameterizable Hermitian operators.
- We propose *Quantum Generator Kernels* (QGKs), a novel kernel method that leverages Hamiltonian-driven unitaries with data-conditioned generator weights.
- We present an in-depth theoretical analysis of the QGK, demonstrating its advantageous expressibility, parameter scaling, and computational complexity properties.
- Extensive empirical validation across binary and multi-class benchmarks, including `MNIST` and `CIFAR10`, shows that QGKs consistently outperform state-of-the-art quantum and classical kernel baselines, even under realistic noise models of current hardware.

2 BACKGROUND

Kernel methods Kernel methods describe a map into a high-dimensional feature space ψ, used to project a d-dimensional data point $x \in \mathbb{R}^d$, into a space, where the distribution of data may then be suitable for linear separation. The kernel function $k(x_i, x_j) = \langle \psi(x_i), \psi(x_j) \rangle$ can be understood as the pairwise distance on that feature space. As the feature map for all points may be computationally expensive, it can be important to reduce the number of calls to that function. The *kernel trick* allows for calculating pairwise distances in the feature space without explicitly calculating the feature function. This is possible, for example, if the kernel is a positive definite map, independent of its dimension (Hofmann et al., 2008). The pairwise distances $k(x_i, x_j)$ can be used in a *support vector machine* (SVM) to solve a classification problem. SVMs turn the classification problem into a quadratic optimization problem, defined on pairwise distances using the kernel trick:

$$\arg\min_{\boldsymbol{\alpha}} \frac{1}{2} \sum_{\substack{i=1 \\ j=1}}^{n} \boldsymbol{\alpha}_i \boldsymbol{\alpha}_j y_i y_j k(x_i, x_j) - \sum_{i=1}^{n} \boldsymbol{\alpha}_i \tag{1}$$

where $\boldsymbol{\alpha}$ are the parameters of the support vector machine and y are the labels of n datapoints. The quality of a feature map can be measured and adjusted to provide a better data embedding structure using kernel target alignment (KTA) (Cristianini et al., 2001). KTA quantifies the similarity between a computed kernel matrix and an ideal target kernel, e.g., derived from the class labels.

Quantum computation Quantum systems are described by quantum states, represented as complex vectors encoding observables like spin or position. A single qubit can be written as $|q\rangle = \boldsymbol{\alpha} |0\rangle + \beta |1\rangle$, where $\boldsymbol{\alpha}, \beta \in \mathbb{C}$. Quantum operations on these states are unitary transformations $\boldsymbol{U}$ such that $|\Psi'\rangle = \boldsymbol{U} |\Psi\rangle$. In practice, these are decomposed into elementary one- and two-qubit gates and executed on quantum hardware. Measurement collapses the quantum state into classical outcomes Nielsen & Chuang (2010). Mathematically, such operations form the special unitary group $SU(N)$ for $N = 2^\eta$ qubits. As a Lie group, $SU(N)$ has a corresponding Lie algebra $\mathfrak{su}(N)$, a real vector space of skew-Hermitian, trace-zero matrices Hall (2013). The elements of the Lie algebra, known as generators, define the fundamental directions in which unitary quantum operations can be constructed. Since the Lie algebra forms a linear vector space, multiple generators can be combined additively to form complex Hermitian operators. These operators are then mapped to unitary matrices via the exponential map, $\exp\colon \mathfrak{su}(N) \to SU(N)$. In quantum computing, a natural basis for this algebra is the Pauli basis, consisting of tensor products of $\sigma_x, \sigma_y, \sigma_z, \mathbb{1}$: These form the building blocks for quantum circuits and support gradient-based learning due to their manifold structure.

Quantum Kernel Methods A central difference in a system of η qubits compared to classical bits is that the dimension of the mathematical space of η qubits scales exponentially in η. Formally, the state of a system of qubits is a ray in a *Hilbert space*, which is generally expressed by $\mathbb{C}^{2^\eta}$. This exponential scaling motivates the quantum kernel method, in which the Hilbert space is used as the feature space, analogous to conventional kernel methods (Mengoni & Di Pierro, 2019). As shown in (Schuld et al., 2021a), a large class of supervised quantum models are kernel methods. A deeper analysis of the mathematical structure of data embedding in quantum circuits shows that combining data uploading with parameterized quantum gates allows for arbitrary function approximation in the form of a Fourier series (Schuld et al., 2021b).

3 VARIATIONAL GENERATOR GROUPS

Information can be encoded into a quantum system either by initializing a quantum state with free parameters or by applying a parameterized operator to a fixed initial state. Given the limited qubit counts in current NISQ hardware, we aim to maximize parameter density per qubit. A common quantum encoding approach, known as amplitude encoding, embeds classical data directly into a state vector within a 2^η-dimensional Hilbert space, where each entry represents a complex amplitude (Biamonte et al., 2017). Accounting for both the real and imaginary components as well as the normalization constraint, this allows for a total of $2^{\eta+1} - 1$ free parameters. An alternative and more hardware-friendly variant is rotational (angle) encoding, where classical values are mapped to the rotation angles of single-qubit gates (e.g., $R_x(\boldsymbol{\theta})$), applied to each qubit independently. While this method is easier to implement and preserves data locality, it significantly limits the expressiveness of the encoding, scaling only linearly with the number of qubits. In contrast, encoding classical data via a unitary operator acting on a quantum state leverages the full expressive power of the Lie algebra $\mathfrak{su}(2^\eta)$, which offers up to $2^{2\eta} - 1$ free parameters. This yields an exponential increase in representational capacity (by a factor of $2^{\eta-1}$) over state-based encoding, offering significantly greater flexibility and expressivity for quantum learning tasks.

This insight motivates our approach: rather than embedding data directly into a quantum state, we build unitary operators from structured combinations of algebraic generators. Specifically, we construct a complete and well-behaved set of Hermitian generators that span a subalgebra of $\mathfrak{su}(2^\eta)$. These generators are derived systematically to ensure linear independence, closure under commutation, and coverage of all valid operator directions in the Hilbert space. The full derivation and construction procedure are detailed in Appendix A, including Alg. 2 outlining the algorithmic formulation. Overall, this construction yields a complete and hardware-compatible generator basis for building expressive and efficient quantum kernels, as formally stated in the following theorem.

Theorem 3.1. *Let $\mathfrak{H}$ be the set of Hermitian generators constructed as described in Alg. 2. Then $\mathfrak{H}$ spans a Lie subalgebra $\mathfrak{h} \subseteq \mathfrak{su}(2^\eta)$ that is closed under commutation, linearly independent, and expressible in terms of Pauli basis elements, ensuring both algebraic validity and implementability on quantum hardware.*

Proof. The generator set $\mathfrak{H}$ is constructed from three families of Hermitian matrices: off-diagonal real symmetric matrices (Eq. 13), off-diagonal purely imaginary anti-symmetric matrices (Eq. 14), and diagonal traceless real matrices (Eq. 15). Together, these matrices span the entire space of traceless Hermitian operators on $\mathbb{C}^{2^\eta}$, yielding $4^\eta - 1$ linearly independent elements, which matches the dimension of the Lie algebra $\mathfrak{su}(2^\eta)$. Their construction guarantees closure under the commutator operation, fulfilling the necessary condition for forming a Lie subalgebra $\mathfrak{h} \subseteq \mathfrak{su}(2^\eta)$. Moreover, since the Pauli basis forms a complete operator basis of $\mathfrak{su}(2^\eta)$, each Hermitian generator $h_k \in \mathfrak{H}$ can be decomposed as a real linear combination of Pauli basis elements. This establishes a direct correspondence between our generator-based formalism and standard quantum circuit implementations, where unitary operations are constructed from Pauli rotations. □

This implies that any unitary generated by h_k can, in principle, be synthesized into a gate-based quantum circuit using known decomposition techniques. Hence, $\mathfrak{H}$ not only provides complete algebraic coverage for encoding but also ensures practical compatibility with current quantum hardware. With the set of generators $\mathfrak{H}$ in hand, it is now possible to encode a real-valued g-dimensional parameter vector $\boldsymbol{\phi} \in \mathbb{R}^g$ into a sequence of unitary operators. Theoretically, for an 8-qubit system, we could encode $65,535$ parameters into this sequence. Therefore, we propose to merge them into *Variational Generator Groups* (VGGs), combining multiple generators with a single parameter. To do so, we split the list of generators into equally sized partitions. Every group $\mathcal{G} \subset \mathfrak{H}$ constitutes a set of generators linearly combined to form a single Hermitian matrix $\hat{\boldsymbol{H}}_i$, constructed according to Alg. 1, which can be mapped to a unitary operator $\hat{\boldsymbol{U}}$ using the time development of the quantum state, substituting the time dependence by a parameter element $\boldsymbol{\phi}_i$:

$$\hat{\boldsymbol{U}}_{\boldsymbol{\phi}_i} = e^{-i \cdot \boldsymbol{\phi}_i \cdot \hat{\boldsymbol{H}}_i} \tag{2}$$

Algorithm 1 Construction of Variational Generator Groups (VGGs)

Require: Set of generators $\mathfrak{H}$, Number of groups $g \in [1, 2^{2\eta} - 1]$, Projection width $w \in [1, 2\eta]$
Ensure: Hermitian Matrix Groups $\hat{\boldsymbol{H}}$
1: Initialize Hamiltonian matrix: $\hat{\boldsymbol{H}} \leftarrow \mathbf{0}_{(g,H,H)}$
2: Generate generator to group mapping according to the specified width w:
3: $idx \leftarrow \langle (j \cdot 2^w \bmod |\mathfrak{H}|,\ j \bmod g) \quad | \quad j \in \{0, 1, \ldots, |\mathfrak{H}| - 1\} \rangle$
4: **for all** $i \in [0, g[\ , \forall (j, k) \in \text{enumerate}(idx)$ s.t. $j \bmod g = i$ **do**
5: $\quad \hat{\boldsymbol{H}}[i][\mathfrak{H}[k][0]] \leftarrow \hat{\boldsymbol{H}}[i][\mathfrak{H}[k][0]] + \mathfrak{H}[k][1]$ ▷ $[\cdot]$ is used for array indexing here
6: **end for**

By grouping the generators, we are able to define the number of parameters that are introduced into the unitary. We choose the total number of groups g (i.e., the number of embeddable parameters) as:

$$g = \frac{|\mathfrak{H}|}{\Gamma_\eta}\ , \text{with} \qquad \Gamma_\eta = \begin{cases} 2 \cdot \Gamma_{\eta-1} + 1 & \text{if } \eta > 2 \text{ and } \eta \text{ is odd,} \\ 2 \cdot \Gamma_{\eta-1} - 1 & \text{if } \eta > 2 \text{ and } \eta \text{ is even,} \\ 1 & \text{if } \eta \leq 2, \end{cases} \tag{3}$$

to ensure scaling the number of generators per group Γ_η approximately exponentially with the total number of generators $|\mathfrak{H}|$. The grouping process is further parameterized by the projection width w that determines the stride at which generators are assigned to groups. By varying this projection width, we can control the density of generators per VGG (cf. Fig. 4). Consequently, Alg. 1 ensures an even distribution of generators across all groups. Preliminary studies showed a wide stride (i.e., $w = 1$) to be most promising. Further justification for this approach, including comparisons to ungrouped and fully grouped schemes, is discussed in Appendix B, while the empirical properties of the resulting VGGs are analyzed in Sec. 6.

4 Quantum Generator Kernels

Via this procedure, we create a VGG with a unitary operator $\hat{\boldsymbol{U}}_{\boldsymbol{\phi}_i}$ for every parameter element $\boldsymbol{\phi}_i$, which can be decomposed into quantum gates or applied directly onto an initial quantum state. When multiplying the set of VGGs in a sequence, we obtain one condensed unitary incorporating all parameters $\boldsymbol{\phi}$:

$$\hat{\boldsymbol{U}}_{\boldsymbol{\phi}} = \exp\left(\sum_{i=1}^{g} -i \cdot \boldsymbol{\phi}_i \cdot \hat{\boldsymbol{H}}_i\right) \tag{4}$$

As shown in Eq. equation 19, the group of unitary matrices is closed regarding multiplication; hence, $\hat{\boldsymbol{U}}_{\boldsymbol{\phi}}$ must also be unitary. We refer to this unified operator $\hat{\boldsymbol{U}}_{\boldsymbol{\phi}}$ as the *Quantum Generator Kernel* (QGK), illustrated in Fig. 1, which is applied via

$$\psi(x) = \hat{\boldsymbol{U}}_x \left|\Psi\right\rangle = \left|\Psi'\right\rangle \tag{5}$$

to the totally mixed initial state $\langle\Psi|$, generated starting from the ground state $\langle 0|$ using $\otimes_{i=1}^{\eta} \mathcal{H} \left|0\right\rangle = \left|\Psi\right\rangle$, with η qubits and the Hadamard gate $\mathcal{H}$ applied to all qubits. To calculate the kernel matrix $\boldsymbol{K}$ from our QGK, we use the fidelity as the distance between the states:

$$\boldsymbol{K} = k(x_i, x_j) = \left|\langle\Psi| \hat{\boldsymbol{U}}_{x_j}^{\dagger} \hat{\boldsymbol{U}}_{x_i} \left|\Psi\right\rangle\right|^2 \tag{6}$$

To embed data using the QGK (cf. Fig. 1, phase 1), we can either use the input data to parameterize the VGGs directly, i.e., $\boldsymbol{\phi} = x \in \mathbb{R}^d$ as denoted in Eq. equation 5, or use a feature extractor $\mathcal{F}_{\boldsymbol{\theta}} : \mathbb{R}^d \mapsto \mathbb{R}^g$, parameterized by $\boldsymbol{\theta}$, s.t. $\boldsymbol{\phi} = \mathcal{F}_{\boldsymbol{\theta}}(x)$. Note that to directly embed input data, the number of groups g must be set according to the input dimension d. However, when using a feature extractor, we can decouple the input dimension from the number of generator groups. This enables dimensionality reduction, which we quantify via the compression factor $\gamma = d/g$. With the embedded data, the kernel matrix can be used to fit a support vector machine (SVM) parameterized by $\boldsymbol{\alpha}$ according to Eq. equation 1, to perform arbitrary binary classification tasks.

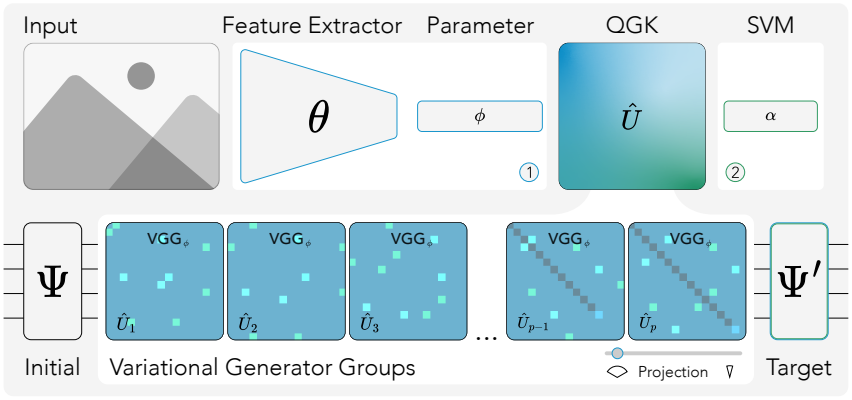

Figure 1: Quantum Generator Kernel: A generator-based quantum kernel architecture based on VGGs for parameterizable projection. Each colored matrix corresponds to one of $g = 51$ *Variational Generator Groups* (VGGs) merged for $\eta = 4$ qubits, visualized as heatmaps of the magnitude (blue) and phase (green) of the resulting generators merged into the operator. The QGK is parameterized by the context $\boldsymbol{\phi}$, which is either given directly by the input or extracted from the input using a feature extractor, adapted during the pre-training phase (1) by updating the parameters $\boldsymbol{\theta}$ to minimize the Kernel-Target Alignment (KTA) loss. In phase (2), a support vector machine (SVM), parameterized by $\boldsymbol{\alpha}$, is trained using the resulting QGK $\hat{\boldsymbol{U}}$.

To pre-train the parameterization $\boldsymbol{\theta}$ of the feature extractor, we suggest using the Kernel Target Alignment (KTA) loss, as suggested in (Hubregtsen et al., 2022):

$$\mathcal{L}_{\text{KTA}} = 1 - \frac{\text{Tr}(\boldsymbol{K}\boldsymbol{Y})}{\|\boldsymbol{K}\|_{\text{F}} \cdot \|\boldsymbol{Y}\|_{\text{F}}}, \tag{7}$$

with the kernel matrix $\boldsymbol{K}$ and the classification targets $\boldsymbol{Y}$, where $\text{Tr}(\boldsymbol{A})$ is the trace of matrix $\boldsymbol{A}$ and $||\boldsymbol{A}||_{\text{F}}$ is the Frobenius norm.

5 Related Work

Embedding Processes To encode classical data into quantum systems, various strategies have been developed, ranging from fixed mappings such as *basis encoding*, where binary values $b \in \{0, 1\}$ are mapped to computational basis states $|b\rangle$, to more compact methods such as *amplitude encoding*, where a normalized vector $v \in \mathbb{R}^{2^\eta}$ is embedded directly into the amplitudes of a quantum state $|\Psi\rangle$. While amplitude encoding uses only η qubits to represent exponentially large vectors, its practical use is limited due to costly state preparation and reduced kernel expressivity unless followed by complex unitaries (Sun et al., 2023; Schuld et al., 2021b; Schuld & Killoran, 2019; Huang et al., 2021). *Angle encodings*, or Pauli rotational embeddings, instead map real-valued inputs into single-axis rotations such as $R_X(x)$ or $R_Z(x)$, and form the basis of many variational quantum circuits. Their expressivity is often enhanced by *data reuploading* (Pérez-Salinas et al., 2020), which introduces nonlinearity through repeated injection of inputs, enabling the circuit to approximate Fourier-like transformations (Jaderberg et al., 2024). The Quantum Embedding Kernel (QEK) (Hubregtsen et al., 2022) leverages this mechanism to train kernel functions via KTA maximization. However, such methods rely on axis-aligned encodings and fixed circuit structures. In contrast, our generator-based approach generalizes the rotational encoding paradigm by constructing unitaries from grouped, algebraically structured combinations of Hermitian generators $\hat{\boldsymbol{H}}_k = \sum_{h \in \mathcal{G}_k \subset \mathfrak{H}} h$, where each h is a linear combination of Pauli strings from the full Pauli basis (cf. Theorem 3.1). The resulting unitary transformations $\exp(-i\boldsymbol{\phi}_k \hat{\boldsymbol{H}}_k)$ support group-level, multi-axis parameterization over $\mathfrak{su}(2^\eta)$, enabling dense, scalable, and hardware-compatible embeddings that preserve differentiability and extend far beyond the capacity of traditional axis-aligned encodings. This structured construction allows for greater expressivity per qubit, making it particularly effective for kernel learning in qubit-constrained settings.

Hybrid QML Motivated by the limited capabilities of current quantum hardware, hybrid quantum-classical machine learning approaches have been explored in literature, which add pre- and postprocessing layers to the quantum model (Mari et al., 2020). While this approach allows the exploration of problems that are beyond the capabilities of current quantum hardware by handling larger data sizes, it blurs the individual contributions of the classical and the quantum components to the overall solution quality (Altmann et al., 2023; Kölle et al., 2024). A recent example combining the above principles is the *Hardware Efficient Embedding* (HEE) (Thanasilp et al., 2024), where input-dependent rotations are arranged in layered circuits interleaved with entangling gates (e.g., CNOT or CZ). These embeddings are expressive and compatible with near-term devices, but they can lead to exponentially concentrated kernel values and barren features unless carefully controlled. To adapt the input dimensionality to the limited number of qubits, the authors apply principal component analysis (PCA). Even though the input dimensionality of our proposed generator-based approach scales exponentially with the number of qubits, in contrast to the linear scaling of the HEE, its preprocessing denotes a similar approach to the linear layer we introduce. However, rather than static feature extraction, we further use this pre-processing to pre-train the projection of the kernel.

Generator-based approaches The exploration of generator-based quantum computing is rather recent, compared to the longer exploration of gate-based variational circuits (Nielsen & Chuang, 2010). Generators are used in more mathematical explorations of quantum computing (Mansky et al., 2023a). In particular, they are found in the treatment of barren plateaus (Arrasmith et al., 2021; Goh et al., 2023; Ragone et al., 2024) and specialized circuits that focus on restricting subspaces (Schatzki et al., 2024; Nguyen et al., 2024; Mansky et al., 2023b). A direct equivalent to the generators does not exist in classical machine learning, owing to the different mathematical structure (Bronstein et al., 2021).

6 Empirical Analysis

In this section, we aim to provide an empirical analysis of the resulting properties of the proposed *Quantum Generator Kernel* (QGK) and compare them to the *Quantum Embedding Kernel* (QEK) as a representative state-of-the-art approach to quantum kernel methods. Fig. 2 summarizes our results.

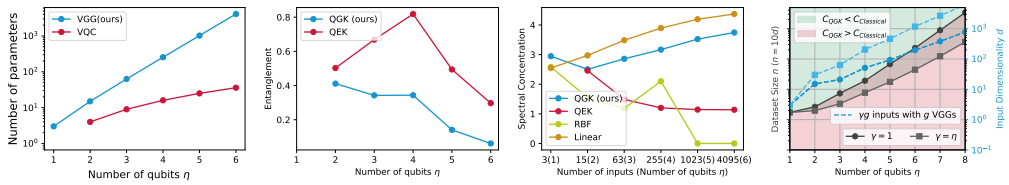

(a) Parameters (b) Entanglement (c) Expressibility (d) Complexity

Figure 2: Comparing the scaling behavior of the QGK to classical and quantum kernels w.r.t. the number of available qubits η (i.e., $4^\eta - 1$ input dimensions), regarding: (a) the number of available parameters, (b) the entanglement capability by means of the Meyer-Wallach measure, (c) the expressibility by means of the spectral concentration, and (d) the computational complexity, showing the complexity breakeven dataset size n when classically simulating the QGK (left y-axis) and the number of VGGs and resulting inputs (right y-axis, blue), scaled to $n = 10d$ to satisfy $n \gg d$.

Parameter efficiency Fig. 2a shows the scalability of the number of parameters w.r.t. the number of qubits. For the VQC, we assume a maximum of η^2 input parameters, i.e., using η layers to embed the input data, scaling quadratically with the number of qubits. Utilizing generators in Hilbert space rather than fixed gate-based embedding processes, our approach shows significantly improved qubit efficiency, scaling exponentially with the number of qubits. Thus, QGK offers an overall higher data capacity, which is especially crucial for realizing real-world applications on near-term quantum devices. To ensure a fair comparison with equal parameter counts, the following analysis is based on the maximum number of QGK parameters, where the QEK is extended by parameterized reuploading layers to replenish the additional parameters.

Kernel properties Fig. 2b shows the maximum entanglement capabilities by means of the Meyer-Wallach measure. Here, the embedding-based approach shows higher capabilities, due to the entanglement layers. For both approaches, the entanglement capability peaks at lower qubit numbers and steadily decreases afterwards. However, given that strong entanglements might also impede optimization, this property could actually be beneficial to both approaches. Fig. 2c compares the spectral concentration of various kernels as a measure of expressibility. The QGK shows a clear upward trend with increasing qubit count, benefiting from its generator-based structure and high parameter density. In contrast, the QEK exhibits decreasing expressibility, suggesting weaker scalability with added parameters. The classical RBF kernel also shows decreasing spectral concentration with increasing input size, while the Linear kernel, similar to QGK, increases steadily. Notably, QGK maintains lower spectral divergence than the Linear kernel across input sizes despite operating in exponentially larger Hilbert spaces, indicating strong resilience against expressibility collapse and exponential concentration. These results highlight QGK's favorable expressibility-to-learnability trade-off, making it a scalable and efficient alternative for hybrid quantum-classical pipelines.

Computational Complextiy Despite the exponential scaling in qubit number η, the QGK remains classically simulable due to its decomposition into tensor-efficient operations: generator construction, input projection, quantum evolution, and pairwise kernel evaluation. Unlike classical kernels such as RBF or Linear, which incur $\mathcal{O}(n^2 \cdot d)$ cost for computing the similarity matrix, QGK scales as $\mathcal{O}(4^\eta + n \cdot \gamma \cdot g^2 + n \cdot 8^\eta + n^2 \cdot 2^\eta)$, with g VGGs and the compression ratio $\gamma = d/g$. This structure favors sample-efficient scenarios revealed by the complexity analysis shown in Fig. 2d, indicating two key properties of the QGK: (i) for low qubit number ($\eta \leq 5$) QGK offers a computational advantage over classical kernels when using a 1:1 mapping ($\gamma = 1$). (ii) to enable larger-scale applications (e.g., $d > 100$) efficiently, hybrid approaches with $\gamma > 1$ are required to compress the input. E.g., using $\gamma = \eta$ pushes the lower efficiency bound further down, such that the input dimension reference ($d = \eta g$ for g VGGs, light blue) does not intersect anymore. This hybrid execution enables scalable and classically feasible QGK training in the NISQ era and lays the groundwork for full quantum execution on future fault-tolerant architectures. A detailed analysis, including complexity thresholds, approximations, and formal bounds, is provided in Appendix C.

7 EVALUATION

Setup To empirically validate the properties and advantages discussed above, this section demonstrates the kernels' trainability, scalability, and hardware applicability across various tasks. We use the `moons` and `circles` datasets from (Pedregosa et al., 2011), with $d = 2$ input features each, both augmented with 20% noise and the `bank` (Moro et al., 2014a;b) dataset with $d = 16$ input features as small-scale synthetic and real-world benchmarks with $n = 200$, and the 10-class `MNIST` (LeCun et al., 1998) ($d = 784$) and `CIFAR10` (Krizhevsky et al., 2009) ($d = 3072$) datasets with $n = 1000$, to demonstrate scalable real-world applicability. In addition to the QEK (Hubregtsen et al., 2022) and HEE (Thanasilp et al., 2024), we evaluate *Radial Basis Functions* (RBF) and *Linear Kernels* as classical state-of-the-art baselines. To ensure approximately even capabilities, the QEK and HEE circuits comprise one data-reuploading layer, i.e., $2 \cdot d/\eta$ layers parameterized by Y- and CZ-rotations for the QEK, and 2 X-rotational input embedding layers for the HEE. To parameterize the feature projection of the QGK, we use a single linear layer. To provide an ablation quantifying the impact of using KTA to train the kernel, we also report the untrained QGK performance (*QGK Static*). To additionally quantify the impact of the VGG-based kernel itself and delimit it from the classical preprocessing, we adapted our linear pre-processing to the HEE (*HEE Linear*), whereas *HEE* refers to the untrained approach using PCA for feature extraction. We pre-train the embedding parameterization for 100 epochs using the Adam optimizer with learning rate $10^{\eta-1}$. Unless stated otherwise, we use $\eta = 2$ for the binary and $\eta = 5$ for the multi-class benchmarks. As a general performance metric, we use the classification accuracy on an unseen 10% test-split, additionally reporting the *Kernel Target Alignment* (KTA). All results are averaged over eight random seeds with 95% confidence intervals. Non-pretrained approaches are shown as dashed horizontal lines. All evaluations were conducted on Apple M2 Ultra hardware with 192GB memory and a total compute time of approximately 96 hours using torchquantum (Wang et al., 2022) [1].

[1]The required implementations are appended and will be open-sourced upon publication.

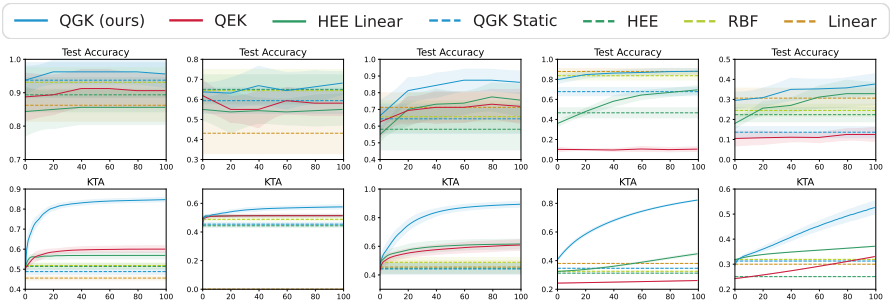

(a) moons (b) circles (c) bank (d) MNIST (e) CIFAR10

Figure 3: Training performance of the QGK(blue), QEK(red), HEE(green), RBF(yellow), and Linear(orange) Kernels w.r.t. the Test Accuracy (left) and KTA (right) in the moons, circles, bank, MNIST, and CIFAR10 benchmarks, with the QGK outperforming all compared approaches.

Binary Classification The training results for the moons dataset are shown in Fig. 3a. Notably, QGK outperforms both embedding-based approaches. Training the projection increases the final test accuracy from 94% to 96%, and even outperforms both classical approaches, with a final KTA above 0.8. Similar performance trends are prevalent in the circles benchmark shown in Fig. 3b, where the QGK outperforms all compared approaches, including both quantum and classical baselines. The overall higher accuracy compared to the HEE Linear ablation further underscores the effectiveness of our generator-based kernel over embedding-based alternatives. Looking at the results for the real-world bank dataset in Fig. 3c, the QGK continues to expand its performance lead. Despite the increased complexity introduced by the 16-dimensional input space, it achieves a mean final test accuracy of 86%, significantly outperforming all competing methods. This highlights QGK's ability to maintain robustness and accuracy even in higher-dimensional, non-trivial learning tasks.

Large-Scale Tasks To evaluate the scalability of the Quantum Generator Kernel (QGK), we investigate its performance on the 10-class MNIST and CIFAR10 benchmarks, shown in Fig. 3d and Fig. 3e. On MNIST, QGK achieves a final test accuracy of around 88%, matching the performance of the best classical method (Linear), and significantly outperforming QEK and HEE. Even without any trained projection, QGK Static achieves strong performance, highlighting the expressive nature of the generator-based representation. On CIFAR10, a considerably more challenging dataset ($d = 3072$), QGK still achieves the highest accuracy among all tested kernels around 0.38%, despite the strong compression required for five-qubit compatibility. In contrast, both quantum baselines (QEK, HEE) and classical kernels (RBF, Linear) show limited performance under the same constraints. These results illustrate the strong adaptability of QGK under large input dimensionality and its ability to generalize beyond synthetic or low-dimensional tasks.

Hardware Compatibility To assess compatibility with current quantum hardware and evaluate robustness to noise, we compiled all compared circuits to IBM's Falcon architecture and simulated them using realistic noise models[2]. As summarized in Tab. 1, for the binary classification tasks, all methods maintain manageable depths below 100, allowing realistic simulation under noise. Notably, QGK outperforms all compared approaches (including both classical ones) even when executed under realistic hardware noise. On larger-scale tasks, the compiled depths diverge, reflecting significant differences in the encoding strategies (cf. Tab. 3). HEE achieves the lowest depth but only encodes five features (less than 1% of the input dimension, even for the lower-dimensional MNIST), relying heavily on classical preprocessing, arguably limiting its comparability. At the other extreme, QEK encodes all features without classical reduction, but at the cost of unmanageable circuit depths exceeding 20k, demonstrating its poor scalability due to the fixed embedding structure. In contrast, QGK strikes a practical balance: grouping generators to embed 93 features using five qubits yields manageable depths below 5k, without heavy preprocessing. While such depths remain intractable for today's noisy hardware, exhaustive simulation offers limited value and is better reserved for future error-corrected devices. Notably, QGK's structured design allows further depth reductions via generator pruning, paving the way for efficient deployment on fault-tolerant quantum systems.

[2]We use the simulated 5-qubit IBM Falcon processor *FakeQuito* (Javadi-Abhari et al., 2024).

Dataset (d)	QGK (ours)	QEK	HEE	RBF	Linear
moons (2)	$\boldsymbol{0.96 \pm 0.04 (28)}$	$0.91 \pm 0.05 (50)$	$0.89 \pm 0.06 (18)$	0.93 ± 0.04	0.86 ± 0.05
circles (2)	$\boldsymbol{0.69 \pm 0.07 (28)}$	$0.58 \pm 0.09 (50)$	$0.64 \pm 0.06 (18)$	0.64 ± 0.11	0.43 ± 0.10
bank (16)	$\boldsymbol{0.87 \pm 0.06 (28)}$	$0.72 \pm 0.10 (380)$	$0.61 \pm 0.10 (18)$	0.66 ± 0.09	0.71 ± 0.09
MNIST (784)	$\mathbf{0.88 \pm 0.03 (4754)}$	$0.10 \pm 0.02 (24084)$	$0.41 \pm 0.03 (53)$	0.84 ± 0.04	$\mathbf{0.88 \pm 0.03}$
CIFAR10 (3072)	$\mathbf{0.38 \pm 0.05 (4754)}$	$0.09 \pm 0.01 (94485)$	$0.21 \pm 0.03 (53)$	0.24 ± 0.03	0.31 ± 0.05

Table 1: Final test accuracies across five benchmarks, comparing QGK (ours) with quantum (QEK, QGK Static, HEE) and classical (Linear, RBF) kernels. Italic values indicate results obtained from noisy circuit simulation on 5-qubit IBM Falcon hardware (Quito), with the compiled circuit depth in parentheses. Even under hardware noise, QGK consistently achieves the highest accuracy, demonstrating superior robustness and scalability across both synthetic and real-world datasets.

8 Conclusion

In this paper, we introduced *Quantum Generator Kernels* (QGK), a novel generator-based approach to quantum kernel methods. The QGK consists of Variational Generator Groups (VGGs) that merge a set of universal generators into parameterizable groups. Building upon universal generators in Hilbert space, QGKs offer significantly improved parameter scalability compared to common gate-based approaches, employing fixed embedding processes. Empirical studies across five benchmarks demonstrate that the QGK achieves superior trainability and classification accuracy, consistently outperforming quantum baselines and matching or exceeding the best classical methods, even under realistic hardware noise.

Key Results On both synthetic binary tasks, QGK outperforms classical and quantum embedding-based methods, showcasing strong expressiveness under limited quantum resources. On the real-world bank dataset, QGK maintains a clear lead, reaching 87% accuracy despite the 16-dimensional input space. On the larger-scale MNIST benchmark, QGK reaches 88% accuracy, matching the best classical kernel (Linear) and significantly outperforming both quantum baselines. On the more complex CIFAR10, QGK achieves 38%, clearly surpassing QEK (9%), HEE (21%), and even classical kernels like RBF (24%) and Linear (31%). These results highlight QGK's strong scalability, embedding efficiency, and superior learning capacity under high-dimensional input conditions. Despite limited qubit budgets, QGK provides expressive embeddings through generator-grouped unitaries, offering a practical trade-off between depth, accuracy, and embedding richness.

Limitations Although generator-based quantum kernels provide strong theoretical expressiveness and favorable scaling, they are not natively supported on current hardware. Combined with today's limited quantum device capabilities, this constrains their immediate large-scale deployment. At the same time, this early stage presents an opportunity for application-driven co-design that may enable native execution of generator-based models in the future. To assess near-term viability, we compiled QGK circuits to current IBM hardware and simulated them under realistic noise. On small-scale tasks, compiled depths remain well below 100 gates, confirming competitive feasibility relative to conventional gate-based methods. Notably, QGK maintains leading accuracy over both classical and quantum baselines even under noise for all evaluated tasks. For large-scale datasets, however, compiled depths exceed the capabilities of current noisy hardware. Here, efficient tensor-based implementations combined with compression provide competitive classical execution until fault-tolerant quantum devices capable of handling large-scale embeddings become available. Additional efficiency gains may be achieved through generator pruning, further reducing depth.

Outlook For small- and medium-scale tasks, hybrid execution offers a practical path: classical preprocessing can reduce dimensionality before quantum embedding, enabling robust performance on today's noisy devices. For large-scale datasets such as MNIST or CIFAR-10, efficient tensor-based implementations provide a tractable classical alternative, keeping generator-based kernels competitive until quantum hardware matures and even outperforming classical baselines like RBF and Linear. In the long term, with the advent of fault-tolerant systems, QGK could be executed fully quantum, including variational training of projections and native generator-based operations. Overall, QGK provides a scalable, expressive, and classically efficient kernel method for near-term hybrid deployment, while paving the way toward a generator-based paradigm of quantum-native learning in future hardware generations.

Ethics Statement

This work adheres to the ICLR Code of Ethics. It does not involve human subjects, personal data, or sensitive information. Large language models (LLMs) were used solely to assist with language editing and structuring; all technical content and results were developed and verified independently by the authors. We anticipate that advances in quantum machine learning, and in particular the new paradigm of generator-based quantum kernel methods introduced here, may broaden the applicability of kernel learning and enable scalable use of quantum resources in future AI systems.

Reproducibility Statement

We have taken several measures to ensure reproducibility of our results. A detailed description of the proposed Quantum Generator Kernel (QGK) method, including generator construction, grouping procedure, and training pipeline, is provided in the main text and Appendix A and Appendix B. Theorems and proofs of the algebraic properties are included in Appendix C. Hyperparameters, datasets, and experimental setups are reported in Sec. 7 and summarized in Tables 3 and 1. Noise simulations and hardware compilation details are given in Appendix D, with compiled depths explicitly reported. All datasets used (`moons`, `circles`, `bank`, `MNIST`, and `CIFAR10`) are publicly available, with preprocessing steps documented in the supplementary materials. For robustness, we report averages over eight random seeds. The full implementation is uploaded in the code appendix for reproducibility during review and will be open-sourced software upon publication.

References

Philipp Altmann, Leo Sünkel, Jonas Stein, Tobias Müller, Christoph Roch, and Claudia Linnhoff-Popien. Sequent: Towards traceable quantum machine learning using sequential quantum enhanced training. In *Proceedings of the 15th International Conference on Agents and Artificial Intelligence - Volume 3: ICAART*, pp. 744–751. INSTICC, SciTePress, 2023. doi: 10.5220/0011772400003393.

Andrew Arrasmith, M. Cerezo, Piotr Czarnik, Lukasz Cincio, and Patrick J. Coles. Effect of barren plateaus on gradient-free optimization, September 2021. URL http://arxiv.org/abs/2011.12245. arXiv:2011.12245.

Ville Bergholm, Juha J. Vartiainen, Mikko Möttönen, and Martti M. Salomaa. Quantum circuits with uniformly controlled one-qubit gates. *Physical Review A*, 71(5):052330, May 2005. doi: 10.1103/PhysRevA.71.052330. Publisher: American Physical Society.

Jacob Biamonte, Peter Wittek, Nicola Pancotti, Patrick Rebentrost, Nathan Wiebe, and Seth Lloyd. Quantum machine learning. *Nature*, 549(7671):195–202, 2017.

Michael M. Bronstein, Joan Bruna, Taco Cohen, and Petar Veličković. Geometric Deep Learning: Grids, Groups, Graphs, Geodesics, and Gauges, May 2021. URL http://arxiv.org/abs/2104.13478. arXiv:2104.13478.

Marco Cerezo, Andrew Arrasmith, Ryan Babbush, Simon C Benjamin, Suguru Endo, Keisuke Fujii, Jarrod R McClean, Kosuke Mitarai, Xiao Yuan, Lukasz Cincio, et al. Variational quantum algorithms. *Nature Reviews Physics*, 3(9):625–644, 2021.

Nello Cristianini, John Shawe-Taylor, André Elisseeff, and Jaz Kandola. On Kernel-Target Alignment. In *Advances in Neural Information Processing Systems*, volume 14. MIT Press, 2001. URL https://proceedings.neurips.cc/paper/2001/hash/1f71e393b3809197ed66df836fe833e5-Abstract.html.

Matthew L. Goh, Martin Larocca, Lukasz Cincio, M. Cerezo, and Frédéric Sauvage. Lie-algebraic classical simulations for variational quantum computing, August 2023. URL http://arxiv.org/abs/2308.01432. arXiv:2308.01432.

Brian C. Hall. Lie Groups, Lie Algebras, and Representations. In Brian C. Hall (ed.), *Quantum Theory for Mathematicians*, Graduate Texts in Mathematics, pp. 333–366. Springer, New York, NY, 2013. doi: 10.1007/978-1-4614-7116-5_16. URL https://doi.org/10.1007/978-1-4614-7116-5_16.

Thomas Hofmann, Bernhard Schölkopf, and Alexander J. Smola. Kernel methods in machine learning. *The Annals of Statistics*, 36(3):1171–1220, June 2008. ISSN 0090-5364, 2168-8966. doi: 10.1214/009053607000000677. URL https://projecteuclid.org/journals/annals-of-statistics/volume-36/issue-3/Kernel-methods-in-machine-learning/10.1214/009053607000000677.full. Publisher: Institute of Mathematical Statistics.

Hsin-Yuan Huang, Michael Broughton, Masoud Mohseni, Ryan Babbush, Sergio Boixo, Hartmut Neven, and Jarrod R McClean. Power of data in quantum machine learning. *Nature communications*, 12(1):2631, 2021.

Thomas Hubregtsen, David Wierichs, Elies Gil-Fuster, Peter-Jan HS Derks, Paul K Faehrmann, and Johannes Jakob Meyer. Training quantum embedding kernels on near-term quantum computers. *Physical Review A*, 106(4):042431, 2022.

Ben Jaderberg, Antonio A. Gentile, Youssef Achari Berrada, Elvira Shishenina, and Vincent E. Elfving. Let quantum neural networks choose their own frequencies. *Phys. Rev. A*, 109:042421, Apr 2024. doi: 10.1103/PhysRevA.109.042421. URL https://link.aps.org/doi/10.1103/PhysRevA.109.042421.

Ali Javadi-Abhari, Matthew Treinish, Kevin Krsulich, Christopher J. Wood, Jake Lishman, Julien Gacon, Simon Martiel, Paul D. Nation, Lev S. Bishop, Andrew W. Cross, Blake R. Johnson, and Jay M. Gambetta. Quantum computing with Qiskit, 2024.

Alex Krizhevsky, Geoffrey Hinton, et al. Learning multiple layers of features from tiny images. 2009.

Michael Kölle, Jonas Maurer, Philipp Altmann, Leo Sünkel, Jonas Stein, and Claudia Linnhoff-Popien. Disentangling quantum and classical contributions in hybrid quantum machine learning architectures. In *Proceedings of the 16th International Conference on Agents and Artificial Intelligence - Volume 3: ICAART*, pp. 649–656. INSTICC, SciTePress, 2024. doi: 10.5220/0012381600003636.

Yann LeCun, Léon Bottou, Yoshua Bengio, and Patrick Haffner. Gradient-based learning applied to document recognition. *Proceedings of the IEEE*, 86(11):2278–2324, 1998.

Maximilian Balthasar Mansky, Santiago Londoño Castillo, Victor Ramos Puigvert, and Claudia Linnhoff-Popien. Near-optimal quantum circuit construction via Cartan decomposition. *Physical Review A*, 108(5):052607, November 2023a. doi: 10.1103/PhysRevA.108.052607. Publisher: American Physical Society.

Maximilian Balthasar Mansky, Santiago Londoño Castillo, Victor Ramos Puigvert, and Claudia Linnhoff-Popien. Permutation-invariant quantum circuits, December 2023b. URL http://arxiv.org/abs/2312.14909. arXiv:2312.14909.

Maximilian Balthasar Mansky, Victor Ramos Puigvert, Santiago Londoño Castillo, and Claudia Linnhoff-Popien. Decomposition Algorithm of an Arbitrary Pauli Exponential Through a Quantum Circuit. In *2023 IEEE International Conference on Quantum Computing and Engineering (QCE)*, volume 01, pp. 434–442, September 2023c. doi: 10.1109/QCE57702.2023.00056.

Maximilian Balthasar Mansky, Miguel Armayor Martinez, Alejandro Bravo de la Serna, Santiago Londoño Castillo, Dimitra Nikoladou, Gautham Sathish, Zhihao Wang, Sebastian Wölckert, and Claudia Linnhoff-Popien. Scaling of symmetry-restricted quantum circuits, June 2024. URL http://arxiv.org/abs/2406.09962. arXiv:2406.09962.

Andrea Mari, Thomas R. Bromley, Josh Izaac, Maria Schuld, and Nathan Killoran. Transfer learning in hybrid classical-quantum neural networks. *Quantum*, 4:340, October 2020. ISSN 2521-327X. doi: 10.22331/q-2020-10-09-340. URL https://doi.org/10.22331/q-2020-10-09-340.

Jarrod R McClean, Sergio Boixo, Vadim N Smelyanskiy, Ryan Babbush, and Hartmut Neven. Barren plateaus in quantum neural network training landscapes. *Nature communications*, 9(1):4812, 2018.

Riccardo Mengoni and Alessandra Di Pierro. Kernel methods in quantum machine learning. *Quantum Machine Intelligence*, 1(3):65–71, 2019.

Sérgio Moro, Paulo Cortez, and Paulo Rita. A data-driven approach to predict the success of bank telemarketing. *Decision Support Systems*, 62:22–31, 2014a.

Sérgio Moro, Paulo Rita, and Paulo Cortez. Bank Marketing. UCI Machine Learning Repository, 2014b. URL https://doi.org/10.24432/C5K306.

Quynh T. Nguyen, Louis Schatzki, Paolo Braccia, Michael Ragone, Patrick J. Coles, Frédéric Sauvage, Martín Larocca, and M. Cerezo. Theory for Equivariant Quantum Neural Networks. *PRX Quantum*, 5(2):020328, May 2024. doi: 10.1103/PRXQuantum.5.020328. Publisher: American Physical Society.

Michael A. Nielsen and Isaac L. Chuang. *Quantum computation and quantum information*. Cambridge University Press, Cambridge ; New York, 10th anniversary ed edition, 2010. ISBN 978-1-107-00217-3.

Fabian Pedregosa, Gaël Varoquaux, Alexandre Gramfort, Vincent Michel, Bertrand Thirion, Olivier Grisel, Mathieu Blondel, Peter Prettenhofer, Ron Weiss, Vincent Dubourg, et al. Scikit-learn: Machine learning in python. *Journal of machine learning research*, 12(Oct):2825–2830, 2011.

Adrián Pérez-Salinas, Alba Cervera-Lierta, Elies Gil-Fuster, and José I Latorre. Data re-uploading for a universal quantum classifier. *Quantum*, 4:226, 2020.

John Preskill. Quantum computing in the nisq era and beyond. *Quantum*, 2:79, 2018.

Michael Ragone, Bojko N Bakalov, Frédéric Sauvage, Alexander F Kemper, Carlos Ortiz Marrero, Martín Larocca, and M Cerezo. A lie algebraic theory of barren plateaus for deep parameterized quantum circuits. *Nature Communications*, 15(1):7172, 2024.

Louis Schatzki, Martín Larocca, Quynh T. Nguyen, Frédéric Sauvage, and M. Cerezo. Theoretical guarantees for permutation-equivariant quantum neural networks. *npj Quantum Information*, 10 (1):1–14, January 2024. ISSN 2056-6387. doi: 10.1038/s41534-024-00804-1. Publisher: Nature Publishing Group.

Maria Schuld and Nathan Killoran. Quantum machine learning in feature hilbert spaces. *Physical review letters*, 122(4):040504, 2019.

Maria Schuld, Francesco Petruccione, Maria Schuld, and Francesco Petruccione. Quantum models as kernel methods. *Machine Learning with Quantum Computers*, pp. 217–245, 2021a.

Maria Schuld, Ryan Sweke, and Johannes Jakob Meyer. Effect of data encoding on the expressive power of variational quantum-machine-learning models. *Physical Review A*, 103(3):032430, 2021b.

Vivek V. Shende, Stephen S. Bullock, and Igor L. Markov. Synthesis of quantum logic circuits. In *Proceedings of the 2005 Asia and South Pacific Design Automation Conference*, ASP-DAC '05, pp. 272–275, New York, NY, USA, January 2005. Association for Computing Machinery. doi: 10.1145/1120725.1120847.

Xiaoming Sun, Guojing Tian, Shuai Yang, Pei Yuan, and Shengyu Zhang. Asymptotically optimal circuit depth for quantum state preparation and general unitary synthesis. *Trans. Comp.-Aided Des. Integ. Cir. Sys.*, 42(10):3301–3314, October 2023. doi: 10.1109/TCAD.2023.3244885.

Supanut Thanasilp, Samson Wang, Marco Cerezo, and Zoë Holmes. Exponential concentration in quantum kernel methods. *Nature communications*, 15(1):5200, 2024.

Hanrui Wang, Yongshan Ding, Jiaqi Gu, Zirui Li, Yujun Lin, David Z Pan, Frederic T Chong, and Song Han. Quantumnas: Noise-adaptive search for robust quantum circuits. In *The 28th IEEE International Symposium on High-Performance Computer Architecture (HPCA-28)*, 2022.

A Deriving a Universal set of generators

The SU(N) group includes all unitary $N \times N$ matrices under multiplication. As a Lie group, the group elements form a smooth manifold and tangential space, the Lie algebra $\mathfrak{su}(N)$. The Lie algebra itself is defined as an additive real vector space characterized together with a commutator relation, satisfying the Jacobi identity. Further, it exhibits the same dimension as the respective Lie group. The direct connection between elements of a Lie group G and elements of the corresponding Lie algebra $\mathfrak{g}$ can be defined by:

$$\forall_{X \in \mathfrak{g}} \quad e^{-t \cdot X} \in G \quad \text{with } t \in \mathbb{R} \tag{8}$$

However, $X \in \mathfrak{g}$ just holds as long as $\forall_{t \in \mathbb{R}} e^{-t \cdot X} \in G$. The Lie algebra itself constitutes a vector space which is spanned by a number of base elements e_i, while i denotes the respective dimension. The number of base elements is equivalent to the dimension of the Lie algebra. Using the fact that the Lie group G represents a differentiable manifold, the associated Lie algebra $\mathfrak{g}$ represents the tangent space to G at its identity element. This picture leads to the relation given in Eq. equation 9, while the indices l and k denote the application of the equation on a matrix element at the respective position.

$$\frac{\partial}{\partial x_i} A_{lk}(x_1, x_2 ... x_n) \Big|_{x_1=0, x_2=0 ... x_n=0} = (e_i)_{lk} \quad A \in G \tag{9}$$

Since it can be shown that the set of traceless square anti-Hermitian $N \times N$ matrices constitutes the $\mathfrak{su}(N)$ algebra, a complete base set $\{e_1, e_2 ...\}$ of linear independent representatives of $\mathfrak{su}(N)$ is sufficient to create any element within this algebra. By making use of the relation given in Eq. equation 8, we can map any element of $\mathfrak{su}(N)$ to an element of SU(N). Additionally, these anti-Hermitian base elements e_i can be converted into so called Hermitian generator elements h_i by using:

$$e_i = -\frac{1}{2} i \cdot h_i \tag{10}$$

Although directly related to the base elements, the generators do not form a basis of the Lie algebra by themselves. However, in order to create a base element out of a generator, we simply convert Eq. equation 10.

The connection between algebra and group via the algebra is exact (Mansky et al., 2024). It can also be used to build quantum circuits from Lie algebra elements, as every element of the Lie group has a corresponding quantum circuit element. In general, this representation of the group element as a quantum circuit is difficult to find and generally requires 4^η operations to represent (Bergholm et al., 2005; Shende et al., 2005; Mansky et al., 2023a). With the choice of a particular basis, this approach can be simplified. The Pauli basis $\Pi = \bigotimes_i^\eta \{\sigma_x, \sigma_y, \sigma_z, \mathbb{I}\} \backslash \mathbb{I}^\eta$ is the discrete group of Pauli strings, the tensor product of Pauli matrices. This restricts the Lie algebra dimension to $N = 2^\eta$, the natural scaling of qubit-based quantum computers.

The Lie algebra elements can be expanded to quantum circuits mechanistically (Mansky et al., 2023c).

Due to the fact that the group of traceless square anti-Hermitian $N \times N$ matrices constitutes the $\mathfrak{su}(N)$ algebra, a complete set of base elements can be easily formulated. Through the multiplication with a complex factor, Hermitian generators can be constructed following Eq. equation 10. This also makes it possible to start directly by creating a set of base elements for Hermitian matrices (generators) and convert them back to anti-Hermitian matrices by applying the factor. This can be done during the transformation into a unitary displayed in Eq. equation 4.

Firstly, the set of generators $\mathfrak{H}$ needs to show linear independence among all its elements. This can be satisfied if every generator contains at least one element $a_{lk} \neq 0$ for which all other generators show $a_{lk} = 0$. To further ensure that the found generators actually form a basis for Hermitian matrices, any pair of generators h_i and h_j needs to satisfy the following condition:

$$\mathrm{Tr}(h_i, h_j) = 2 \cdot \delta_{ij} \tag{11}$$

Finally, it needs to be ensured that all generators h_i and h_j fulfill the commutator condition characterizing all basis elements of a Lie algebra:

$$[h_i, h_j] = \sum_{k=1}^{n} C_{ikl} \cdot 2i \cdot \ h_k \quad with \ \ \forall_{k \in \{1,2..n\}} h_k \in \mathfrak{H} \ \ \wedge \ \ \forall_{i,k,l} C_{ikl} \in \mathbb{R} \tag{12}$$

Based on these three conditions, the following three generator subsets given in Eqs. equation 13, equation 14, and equation 15 can be found. Here, the first subset defines the off-diagonal real elements, the second one the off-diagonal imaginary elements, and the third set the real diagonal elements.

$$\begin{pmatrix} 0 & 1 & & 0 \\ 1 & 0 & & \\ & & \ddots & \\ 0 & & & 0 \end{pmatrix}, \dots, \begin{pmatrix} 0 & 0 & & 1 \\ 0 & 0 & & \\ & & \ddots & \\ 1 & & & 0 \end{pmatrix}, \dots, \begin{pmatrix} 0 & & & 1 \\ & \ddots & & \\ & & 0 & 1 \\ 0 & & 1 & 0 \end{pmatrix} \tag{13}$$

$$\begin{pmatrix} 0 & -i & & 0 \\ i & 0 & & \\ & & \ddots & \\ 0 & & & 0 \end{pmatrix}, \dots, \begin{pmatrix} 0 & 0 & & -i \\ 0 & 0 & & \\ & & \ddots & \\ i & & & 0 \end{pmatrix}, \dots, \begin{pmatrix} 0 & & & 0 \\ & \ddots & & \\ & & 0 & -i \\ 0 & & i & 0 \end{pmatrix} \tag{14}$$

For the construction of the generators containing diagonal elements, the traceless condition must be regarded. This leads to the construction of a set of matrices given in Eq. equation 15.

$$\begin{pmatrix} 1 & 0 & & 0 \\ 0 & -1 & & \\ & & \ddots & \\ 0 & & & 0 \end{pmatrix}, \dots, \frac{1}{\sqrt{(n-1)!}} \begin{pmatrix} 1 & 0 & & 0 \\ 0 & 1 & & \\ & & \ddots & \\ 0 & & & -(n-1) \end{pmatrix} \tag{15}$$

Algorithmically, the set of generators can be constructed with computational complexity $\mathcal{O}(4^\eta)$ via:

Algorithm 2 Construction of Generators

Require: Number of qubits η
Ensure: Set of generators $\mathfrak{H}$
1: Compute Hilbert space dimension: $H \leftarrow 2^\eta$
2: Initialize empty set $\mathfrak{H}$ and append generators in the format $((\boldsymbol{r}, \boldsymbol{c}), \boldsymbol{v})$,
where $|\boldsymbol{r}| = |\boldsymbol{c}| = |\boldsymbol{v}|$, $\boldsymbol{r}$ and $\boldsymbol{c}$ are lists of indices in the Hamiltonian matrix,
and $\boldsymbol{v}$ is the list of corresponding (non-zero) values of the respective generator.
3: $\mathfrak{H} \leftarrow \mathfrak{H} \cup \{(((\langle r, c\rangle, \langle c, r\rangle), \langle 1 + 0j, 1 + 0j\rangle) \mid \ r \in [0, H[\ , \ \ c \in]r, H[\ \}$
4: $\mathfrak{H} \leftarrow \mathfrak{H} \cup \{(((r, c), (c, r)), (0 + 1j, 0 - 1j)) \mid \ r \in [0, H[\ , \ \ c \in]r, H[\ \}$
5: $\mathfrak{H} \leftarrow \mathfrak{H} \cup \{(((0, \dots, j), (0, \dots, j)), ((1/\sqrt{i!})_j \cup \{-j/\sqrt{i!}\})) \mid \ j \in [1, H[\ \}$

Projection Width Preliminary studies showed a wide stride (i.e., $w = 1$) to be most promising. Fig. 4 shows a visual comparison between wide and narrow projections widths.

B Alternative Grouping Approaches

One alternate approach to form a single unitary matrix incorporating all $2^{2\cdot\eta} - 1$ parameters assigns every free parameter to a specific generator of the underlying $\mathfrak{su}(N)$ algebra. By forming one large linear combination of generators h_i multiplied by the respective parameters $\boldsymbol{\phi}_i$, one Hermitian operator $\hat{\boldsymbol{H}}$ is produced:

$$\hat{\boldsymbol{H}} = \sum_{i=1}^{2^{2\cdot\eta}-1} \boldsymbol{\phi}_i \cdot h_i \quad , \tag{16}$$

while η again corresponds to the number of qubits used. This Hermitian operator $\hat{\boldsymbol{H}}$ can then be converted to a single unitary matrix $\hat{\boldsymbol{U}}$:

$$\hat{\boldsymbol{U}} = e^{-i\hat{\boldsymbol{H}}} = e^{-i\sum_{i=1}^{2^{2\cdot\eta}-1} \boldsymbol{\phi} i h_i} \tag{17}$$

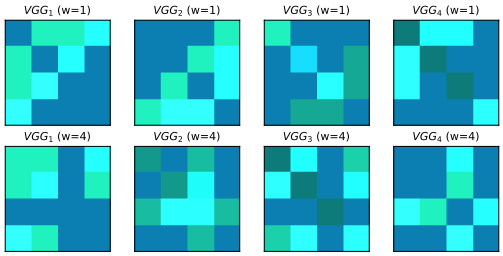

Figure 4: Projection heatmaps for VGGs for $\eta = 2$ qubits, merged in $g = 4$ groups with widths $w = 1$ (upper) and $w = 4$ (lower), visualizing the magnitude (blue) and phase (green) of the resulting generator matrices $\hat{\boldsymbol{H}}$.

An important disadvantage of this approach, however, is the inability to form a finite expression of the derivative of $\hat{\boldsymbol{U}}$ with regard to one of the involved free parameters ϕi in the general case. This issue becomes apparent when differentiating $\hat{\boldsymbol{U}}$ while displaying the involved exponential function in its series representation. The difficulties in forming a finite expression for the derivative originate from the non-commuting characteristic present between specific generators h_i and h_j. An example of this is given in Eq. equation 18:

$$\hat{\boldsymbol{H}} = \sum_{i=1}^{2^{2\cdot\eta}-1} \boldsymbol{\phi}_i \cdot h_k \quad \forall \quad h_k \in \mathcal{G}_i \tag{18}$$

To circumvent the problem, we chose another approach, which enables the formulation of a finite expression of the derivative and which is described in Sec. 3 in more detail. If we separate the set of generators into clusters, assigning one free parameter to every cluster respectively, we generate several unitary sub-operators $\hat{\boldsymbol{U}}_i$, which we contract to a single one according to Eq. equation 4. Since every sub-operator contains only one free parameter, no commutation is necessary in order to form a finite derivative; hence, the non-commuting characteristic does not cause any problems. Also, as given by the following proof showing that the unitary matrices $\boldsymbol{U}$ representing the transformation of a quantum state form a closed group regarding matrix multiplication, the resulting operator is also unitary:

$$\begin{aligned}
\hat{\boldsymbol{U}} = \hat{\boldsymbol{U}}_{\boldsymbol{\phi}_1}\hat{\boldsymbol{U}}_{\boldsymbol{\phi}_2}\dots\hat{\boldsymbol{U}}_{\boldsymbol{\phi}_p} \quad \cap \quad \forall_{i\epsilon\{1\dots p\}} \;\; \hat{\boldsymbol{U}}^+_{\boldsymbol{\phi}_i}\hat{\boldsymbol{U}}_{\boldsymbol{\phi}_i} = \mathbb{I} \\
\implies \hat{\boldsymbol{U}}^+\hat{\boldsymbol{U}} = (\hat{\boldsymbol{U}}_{\boldsymbol{\phi}_1}\hat{\boldsymbol{U}}_{\boldsymbol{\phi}_2}\dots\hat{\boldsymbol{U}}_{\boldsymbol{\phi}_p})^+ \, (\hat{\boldsymbol{U}}_{\boldsymbol{\phi}_1}\hat{\boldsymbol{U}}_{\boldsymbol{\phi}_2}\dots\hat{\boldsymbol{U}}_{\boldsymbol{\phi}_g}) \\
= \hat{\boldsymbol{U}}^+_{\boldsymbol{\phi}_g}\dots\hat{\boldsymbol{U}}^+_{\boldsymbol{\phi}_2}\hat{\boldsymbol{U}}^+_{\boldsymbol{\phi}_1} \cdot \hat{\boldsymbol{U}}_{\boldsymbol{\phi}_1}\hat{\boldsymbol{U}}_{\boldsymbol{\phi}_2}\dots\hat{\boldsymbol{U}}_{\boldsymbol{\phi}_g} \\
= \hat{\boldsymbol{U}}^+_{\boldsymbol{\phi}_g}\dots\hat{\boldsymbol{U}}^+_{\boldsymbol{\phi}_2} \cdot \mathbb{I} \cdot \hat{\boldsymbol{U}}_{\boldsymbol{\phi}_2}\dots\hat{\boldsymbol{U}}_{\boldsymbol{\phi}_g} \\
= \mathbb{I}
\end{aligned} \tag{19}$$

However, maximizing the number of parameters incorporated in $\hat{\boldsymbol{U}}$, i.e., introducing one parameter per generator, requires clusters containing only a single generator, respectively. As a result, we would create one sub-operator per generator. This means we have to do a matrix multiplication for every additional generator in order to get the contracted unitary $\hat{\boldsymbol{U}}$. This again sets a challenge to the approach since the generator number increases exponentially $(2^{2\cdot\eta} - 1)$ with η qubits, making the calculation of $\hat{\boldsymbol{U}}$ computationally expensive. This justifies the implemented flexibility of choosing the size of the used clusters, enabling the adjustment of the tradeoff between computational expense and size of the introduced context.

To additionally reduce the computational complexity of the resulting operators, we furthermore utilize the following approximation:

$$\hat{\boldsymbol{U}}_{\boldsymbol{\phi}} = \exp\left(\sum_{i=0}^{g} -i \cdot \boldsymbol{\phi}_i \cdot \hat{\boldsymbol{H}}_i\right) \approx \prod_{i=0}^{g} \exp\left(-i \cdot \boldsymbol{\phi}_i \cdot \hat{\boldsymbol{H}}_i\right) = \prod_{i=0}^{g} \hat{\boldsymbol{U}}_{\boldsymbol{\phi}_i} \tag{20}$$

C Quantum Generator Kernel Computational Complexity

Despite the exponential scaling in η, the QGK remains classically simulable via efficient tensor operations. To assess the practical efficiency of this approach, we derive the full classical sample complexity of the Quantum Generator Kernel (QGK) and contrast it with classical kernels to determine scalability conditions and break-even points.

Axiom C.1 (QGK Execution Complexity)**.** *Given n samples of d-dimensional inputs, η qubits, and g variational generator groups (VGGs), the cost of executing the QGK kernel is decomposed as:*

- *Generator construction:* $\mathcal{O}(4^\eta)$
- *Input projection* $\boldsymbol{\phi} : \mathbb{R}^d \to \mathbb{R}^g$*:* $\mathcal{O}(n \cdot g \cdot d) = \mathcal{O}(n \cdot \gamma g^2)$
- *Hamiltonian embedding:* $\mathcal{O}(n \cdot 8^\eta)$
- *Kernel matrix computation:* $\mathcal{O}(n^2 \cdot 2^\eta)$

By variablizing the compression ratio $\gamma = \frac{d}{g}$, or, $d = \gamma g$, we can represent the default case of a 1:1 group-to-feature mapping using $\gamma = 1$.

Lemma C.2. *Overall, we can summarize the classical computational complexity of the QGK as:*

$$\mathcal{C}_{QGK} = \mathcal{O}(4^\eta + n \cdot \gamma \cdot g^2 + n \cdot 8^\eta + n^2 \cdot 2^\eta) \tag{21}$$

For comparison, a classical RBF or Linear kernel computes a similarity matrix at $\mathcal{O}(n^2 \cdot d)$. Tab. 2 shows a comparison over the end-to-end complexities of the QGK and Classical Kernels for the utilized benchmarks using a 90/10 train/test split, where QGK is more efficient throughout:

Component	**QGK (ours)**	**Classical Kernel**
moons ($\eta = 2, d = 2, n = 200, g = 15$)	$\mathcal{O}(1.50e+05)$	$\mathcal{O}(6.56e+04)$
circles ($\eta = 2, d = 2, n = 200, g = 15$)	$\mathcal{O}(1.50e+05)$	$\mathcal{O}(6.56e+04)$
Bank ($\eta = 2, d = 16, n = 200, g = 15$)	$\mathcal{O}(1.92e+05)$	$\mathcal{O}(5.25e+05)$
MNIST ($\eta = 5, d = 784, n = 1000, g = 93$)	$\mathcal{O}(1.32e+08)$	$\mathcal{O}(6.43e+08)$
CIFAR10 ($\eta = 5, d = 3072, n = 1000, g = 93$)	$\mathcal{O}(3.45e+08)$	$\mathcal{O}(2.52e+09)$

Table 2: End-to-end complexity comparison between QGK and classical kernels.

To generally determine when the QGK is more efficient than classical kernels, we consider:

$$4^\eta + n \cdot \gamma \cdot g^2 + n \cdot 8^\eta + n^2 \cdot 2^\eta < n^2 \cdot d \tag{22}$$

which can be simplified to the quadratic inequality in n:

$$n^2(2^\eta - \gamma g) + n(\gamma g^2 + 8^\eta) + 4^\eta < 0 \tag{23}$$

which, assuming $A \neq 0$ and $B^2 - 4AC > 0$ (we outline $B^2 \gg 4AC > 0$ below), can be solved to:

$$n > \frac{-B - \sqrt{B^2 - 4AC}}{2A} \quad \text{where} \quad \begin{cases} A = 2^\eta - \gamma g \\ B = \gamma g^2 + 8^\eta \\ C = 4^\eta \end{cases} \tag{24}$$

Summarizing the above derivation, we can determine the lower QGK efficiency bound: $\epsilon b_\gamma = \frac{n}{d}$, where larger intended ratios imply $C_{GQK} < C_{Classical}$ and verce visa. For the default 1:1 group-to-feature mapping ($\gamma = 1$) we therefore get:

η	2	3	4	5	6	7	8
ϵb_1	**1.76**	**3.49**	**3.75**	**7.30**	11.75	23.26	43.75

Using the general assumption $n \gg d$, i.e., favoring high ratios, the above table shows that for low qubit counts classical QGK execution excels classical kernels. For example assuming a minimum dataset-to-input-dimension rate of eight ($\epsilon b_\gamma > 8$), this holds for $\eta \leq 5$ with $\gamma = 1$.

To further facilitate higher qubit counts and larger input dimensionalities, we suggest adapting the input compression γ accordingly. E.g., for $\gamma = \eta$ we get the following approximately constant ratio $\epsilon b_\eta < 1$, which, under the assumption that $n \gg d$, demonstrates that under reasonable compression, executing the QKG classical is computationally more efficient than classical kernels throughout varying numbers of qubits.

η	2	3	4	5	6	7	8
ϵb_η	**0.66**	**0.53**	**0.38**	**0.38**	**0.38**	**0.46**	**0.59**

These findings are summarized in Fig. 2d where the dataset size threshold (n according to Eq. 24) is plotted for $\gamma = 1$ ($\circ$-markers) and $\gamma = 2^\eta$ ($\square$-markers) on the left y-axis. The area above the resulting graphs indicates that classically executing the QGK is more efficient than a classical kernel like RBF or Linear. Combined with the number of generators, dictating the available input dimensions on the right y-axis, scaled to reflect $n \gg d$ ($\gamma g = d = n/10$), the breakeven point regarding the classical complexity can be observed at $\eta \leq 5$ for $\gamma = 1$. Increasing the compression to $\gamma = \eta$ pushes the lower efficiency bound further down, such that the input dimension reference ($d = \eta g$ for g VGGs, light blue) no longer intersects. This demonstrates that such a hybrid approach is an efficient complexity mitigation to enable scalable QGK execution in the current NISQ era, where especially larger quantum systems cannot be efficiently simulated and available quantum hardware is prone to hardware noise. We exemplify this approach with the MNIST and CIFAR10 benchmarks, where, using $\eta = 5$, we have $g = 93$ VGGs, resulting in compression rates of $\gamma \approx 8$ and $\gamma \approx 32$ respectively. Notably, this compression results in a number of groups that show to satisfy the intended ratio of $n = 10d$ between (kernel)-input and dataset dimension, with $d = 1000$.

Overall, we can generalize the above observations in the following two theorems regarding the classical computational complexity of the QGK compared to classical kernels. First, we derive the folwing simplifications and approximations from Eq. 24 based on Theorem C.2:

Lemma C.3 (Simplify complexity bounds)**.** *Given $\gamma \geq 1$, we can show $B^2 \gg 4AC$, or, using $g \approx 3 \cdot 2^\eta$, $(9\gamma \cdot 4^\eta + 8^\eta)^2 \gg 8^\eta(4 - 12\gamma)$, which trivially holds for all $\eta \geq 1$, where, the LHS is largely positive and increasing, while the RHS is negative and decreasing with increasing η. Therefore, we can further approximate:*

$$\frac{-B - \sqrt{B^2 - 4AC}}{2A} \approx \frac{-2B}{2A} = \frac{B}{-A} = \frac{\gamma g^2 + 8^\eta}{\gamma g - 2^\eta} \tag{25}$$

With $d = \gamma g$ and given the number of groups is chosen according to Eq. 3, we can further substitute $g = 3 \cdot 2^\eta - 6 \cdot (\eta \mod 2) + 3 \approx 3 \cdot 2^\eta$, yielding:

$$n > \frac{\gamma g^2 + 8^\eta}{\gamma g - 2^\eta} \approx \frac{9\gamma \cdot 4^\eta + 8^\eta}{3\gamma \cdot 2^\eta - 2^\eta} \tag{26}$$

Thus, ϵb_γ can be further approximated:

$$\epsilon b_\gamma \frac{n}{d} \approx \frac{\frac{9\gamma \cdot 4^\eta + 8^\eta}{3\gamma \cdot 2^\eta - 2^\eta}}{3\gamma \cdot 2^\eta} = \frac{9\gamma \cdot 4^\eta + 8^\eta}{3\gamma(3\gamma - 1) \cdot 4^\eta} \tag{27}$$

These simplifications help us to clearly demonstrate the following theorems:

Theorem C.4. *Classically computing the QGK is more efficient than using a classical kernel such as Linear or RBF, for small qubit numbers of $\eta \leq 5$, when using no compression.*

Proposition C.5. *For fitting kernel classifiers, $n \gg d$ is a generally assumed condition. To determine the efficiency bound, we specifically assume $n = 10d$.*

Proof. Using no compression, i.e.,,$\gamma = 1$, we can derive the following special case from Eq. 27:

$$\epsilon b_1 = \frac{9 \cdot 4^\eta + 8^\eta}{6 \cdot 4^\eta} = \frac{3}{2} + \frac{2^\eta}{6} \tag{28}$$

With $\epsilon b_1 < 10$, we get $2^\eta < 51$, or, $\eta \lessapprox 5.67$. Thus, $n = 10d$ holds for $\eta \leq 5$ with $\gamma = 1$ $\square$

Theorem C.6. *Using sufficient compression, QGKs can be classically executed in a hybrid fashion that is more computationally efficient than classical kernels.*

Proof. To provide a ... we aim to demonstrate finding a compression bound, s.t. $\epsilon b_\gamma < 1$ with $\gamma > 1$. Based on Eq. 27, we rewrite the above condition to:

$$1 > \frac{9\gamma \cdot 4^\eta + 8^\eta}{3\gamma(3\gamma - 1) \cdot 4^\eta} \tag{29}$$

$$0 > 12\gamma - 9\gamma^2 + 2^\eta 0 \tag{30}$$

$$\gamma > \frac{12 + \sqrt{144 + 72 \cdot 2^\eta}}{18} \approx \sqrt{2}^\eta \tag{31}$$

Thus, with sufficient compression, $\gamma > \sqrt{2}^\eta$, we can ensure $\epsilon b_\gamma < 1$, thus, a more efficient classical execution of the QGK in datasets with $n > d$. □

D Additional Results

Dataset	d	Kernel	η	Input Features	Reuploading Layers	Compiled Depth L2	Compiled Depth L1
moons circles	2	QGK (ours)	2	15	-	17	28
		QEK	2	2	1	16	50
		QEK-N	2	2	0	6	26
		HEE	2	2	1	10	18
		HEE-D	2	2	2	10	30
bank	16	QGK (ours)	2	15	-	17	28
		QGK Static	3	16	-	212	248
		QEK	2	16	1	17	380
		QEK-N	2	16	0	17	191
		HEE	2	2	1	10	18
		HEE-D	2	2	2	10	30
MNIST	784	QGK (ours)	5	93	-	4455	4754
		QEK	5	784	0	22709	24084
		QEK-N	5	784	0	11355	12006
		HEE	5	5	1	53	53
		HEE-D	5	5	165	4481	4481
CIFAR10	3072	QGK (ours)	5	93	-	4455	4754
		QGK Static	6	3072	-	18823	19644
		QEK	5	3072	0	88963	94485
		QEK-N	5	3072	0	44461	47223
		HEE	5	5	1	53	53
		HEE-D	5	5	165	4481	4481

Table 3: Parameter Overview: Adapted parameters to ensure comparable prerequisites and capabilities via similar numbers of qubits and compiled circuit depths with level 1 and 2 optimization. Introducing two additional ablations; HEE-D with additional layers, QEK-N without reuploading.

Hardware Considerations Given current and near-term quantum devices, we distinguish three application scenarios for QGK execution. For small-scale datasets and low-depth settings ($\eta < 5$), QGK circuits can be realistically deployed on existing quantum devices. Our simulations confirm noise robustness up to $\sim$ 100 compiled gates, making QGK viable for near-term experimental evaluations. For medium-scale tasks, hybrid execution offers a practical near-term strategy: classical preprocessing can reduce input dimensionality before quantum embedding, enabling robust kernel computation on noisy devices without excessive circuit depth. For large-scale datasets such as MNIST or CIFAR-10, efficient tensor-based implementations with compression provide a tractable classical alternative, ensuring generator-based kernels remain competitive until fault-tolerant systems are available. In the long term, on future fault-tolerant quantum systems, QGK could be implemented end-to-end, including training of linear projection weights via variational optimization, enabling scalable, expressive, and fully quantum kernel learning on large-scale datasets.

A detailed comparison of compiled depths and input dimensionality across QGK and baseline approaches is provided in Tab. 3, illustrating their markedly different scaling behaviors: HEE maintains shallow depths even for higher qubit counts but cannot scale to high-dimensional inputs (since the number of inputs equals the number of qubits), thus heavily relying on classical preprocessing (e.g., PCA for HEE, linear projections for HEE-Linear). QEK, by contrast, adapts to high-dimensional inputs with low qubit counts through reuploading, but this leads to impractical compiled depths as dimensionality grows. QGK offers a compromise, supporting a high number of input features even with few qubits, with compiled depth scaling more favorably while reducing reliance on classical preprocessing.

Finally, Tab. 4 and Tab. 5 report the final test accuracies of all evaluated approaches, under classical execution and simulated hardware noise models, respectively.

Method	`moons` (2)	`circles` (2)	`bank` (16)	`MNIST` (784)	`CIFAR10` (3072)
QGK (ours)	$\mathbf{0.96 \pm 0.04}$	$\mathbf{0.68 \pm 0.06}$	$\mathbf{0.86 \pm 0.07}$	$\mathbf{0.88 \pm 0.03}$	$\mathbf{0.38 \pm 0.05}$
QEK	0.91 ± 0.05	0.58 ± 0.06	0.72 ± 0.10	0.10 ± 0.02	0.12 ± 0.04
QEK-N	0.86 ± 0.05	0.62 ± 0.08	0.64 ± 0.09	0.13 ± 0.02	0.11 ± 0.03
HEE Linear	0.86 ± 0.05	0.55 ± 0.08	0.76 ± 0.10	0.70 ± 0.04	0.33 ± 0.06
QGK Static	0.94 ± 0.05	0.59 ± 0.06	0.64 ± 0.09	0.68 ± 0.04	0.14 ± 0.03
HEE	0.89 ± 0.05	0.65 ± 0.07	0.58 ± 0.12	0.47 ± 0.05	0.22 ± 0.04
HEE-D	0.93 ± 0.03	0.58 ± 0.08	0.58 ± 0.14	0.41 ± 0.03	0.19 ± 0.02
RBF	0.93 ± 0.04	0.64 ± 0.11	0.66 ± 0.09	0.84 ± 0.04	0.24 ± 0.03
Linear	0.86 ± 0.05	0.43 ± 0.10	0.71 ± 0.09	$\mathbf{0.88 \pm 0.03}$	0.31 ± 0.05

Table 4: Final test accuracies for all methods across five benchmarks. The best result per dataset is highlighted in bold. QGK achieves top performance in `moons`, `bank`, `MNIST`, and `CIFAR10`, while Linear matches QGK on `MNIST`.

Method	`moons` (2)	`circles` (2)	`bank` (16)
QGK (ours)	$\boldsymbol{0.96 \pm 0.04\ (28)}$	$\boldsymbol{0.65 \pm 0.12\ (28)}$	$\boldsymbol{0.87 \pm 0.06\ (28)}$
QEK	$0.79 \pm 0.07\ (50)$	$0.49 \pm 0.10\ (50)$	$0.48 \pm 0.10\ (380)$
QEK-N	$0.84 \pm 0.05\ (26)$	$0.54 \pm 0.04\ (26)$	$0.48 \pm 0.10\ (191)$
HEE Linear	$0.51 \pm 0.09\ (18)$	$0.57 \pm 0.08\ (18)$	$0.53 \pm 0.12\ (18)$
QGK Static	$0.93 \pm 0.04\ (28)$	$0.59 \pm 0.04\ (28)$	$0.49 \pm 0.09\ (248)$
HEE	$0.89 \pm 0.05\ (18)$	$0.62 \pm 0.12\ (18)$	$0.61 \pm 0.10\ (18)$
HEE-D	$0.96 \pm 0.03\ (30)$	$0.57 \pm 0.09\ (30)$	$0.60 \pm 0.14\ (30)$

Table 5: Noisy simulation results (compiled depths in parentheses). The best result per dataset is highlighted in bold. A horizontal line separates pre-trained (KTA) approaches from static kernels.